

EFFECTS OF STRONG GRAVITATIONAL LENSING
ON MM-WAVE GALAXY NUMBER COUNTSYASHAR D. HEZAVEH, GILBERT P. HOLDER
Department of Physics, McGill University, Montreal, QC

ABSTRACT

We study the effects of strong lensing on the observed number counts of mm sources using a ray tracing simulation and two number count models of unlensed sources. We employ a quantitative treatment of maximum attainable magnification factor depending on the physical size of the sources, also accounting for effects of lens halo ellipticity. We calculate predicted number counts and redshift distributions of mm galaxies including the effects of strong lensing and compare with the recent source count measurements of the South Pole Telescope (SPT). The predictions have large uncertainties, especially the details of the mass distribution in lens galaxies and the finite extent of sources, but the SPT observations are in good agreement with predictions. The sources detected by SPT are predicted to largely consist of strongly lensed galaxies at $z > 2$. The typical magnifications of these sources depends strongly on both the assumed unlensed source counts and the flux of the observed sources.

Subject headings: gravitational lensing: strong — number counts: individual— finite source effects

1. INTRODUCTION

Many galaxies at redshifts $z \sim 2-5$ have been found to be undergoing large amounts of star formation, leading to a population of distant galaxies with large amounts of warm dust that can be observed at infrared, submm, and mm wavelengths (Blain et al. 2002). Star-forming rates are found to be often in excess of $1000 M_{\odot}/\text{yr}$ (Michałowski et al. 2010), contributing a significant fraction of the total cosmic star formation at these redshifts.

Surveys at submm wavelengths (Coppin et al. 2006) covering smaller areas at high sensitivity have established the existence of a population of dusty star-forming galaxies at high redshift (Blain et al. 2002), showing that the number of sources as a function of flux (the luminosity function) is steeply declining at high fluxes. As a result, gravitational lensing is expected to significantly modify the observed number counts (Blain 1998), an effect known as “magnification” or “amplification” bias (Turner et al. 1984). Recent mm-wave surveys like the South Pole Telescope (SPT; Vieira et al 2010) are now covering enough area to accumulate statistically significant numbers of highly luminous distant galaxies, providing an opportunity to compile large samples of strong gravitational lenses. Recent theoretical work (Negrello et al. 2007; Lima et al. 2009, 2010; Jain & Lima 2010) has demonstrated that gravitational lensing is likely an important contributor to the galaxy counts observed by large scale mm-wave surveys. In addition, evidence is now emerging from Herschel observations (Frayer et al. 2010) that a large fraction of the brightest high-redshift dusty galaxies are indeed strongly lensed.

Much remains unknown about massively star-forming galaxies at high redshift. The redshift distribution as a function of flux is only roughly understood, and different models have very different input physics. For example, the Durham semi-analytic model of galaxy formation requires a top-heavy IMF to explain this population (Lacey et al. 2010). Strong lensing of these sources allows a magnified view, making multi-wavelength follow-

up easier, as the sources are brighter.

In this work we calculate the expected number of strongly lensed galaxies in flux-limited mm-wave surveys, paying particular attention to the expected redshift distribution of the sources and lenses and the effect of finite source effects.

2. OVERVIEW OF CALCULATION OF NUMBER OF
LENSED SOURCES

Determining the expected number of galaxies discovered in mm-wave surveys is complicated by at least four major uncertainties:

- the statistics of the source population (uncertain number counts, uncertain redshift distribution),
- the properties of the source population (uncertain spectral energy distributions, uncertain angular sizes)
- the statistics of the lens population (number counts as a function of mass and redshift)
- the properties of the lens galaxies (internal mass profiles and ellipticities).

To investigate uncertainties in the source population, we use two independent unlensed source count predictions for SPT measurements at 220 GHz (1.4 mm). In particular, the redshift distribution is expected to play a key role in determining lensing efficiencies, so the two different models are intended to provide an estimate of the redshift importance. Our first model, henceforth called the *Durham model*, based on the models developed in Baugh et al. (2005) (Lacey et al. private communication), is the result of semi-analytic modeling of galaxy formation. The second model considered, referred to as the *UBC model* (Marsden, private communication), is obtained through backwards evolution models of the local Universe.

To model the lens population we follow Perrotta et al. (2002), using a Press-Schechter (Press & Schechter 1974) approach to the lens halo distribution as a function of

mass and redshift. We use the Sheth & Tormen (1999) redshift-dependent mass function to model the number of halos of a given mass and redshift for our lens population.

For the internal mass distribution we assume that the region where the majority of strong lensing occurs can be modeled as an elliptical mass profile with a 3D density profile that falls as $1/r^2$. This is an excellent approximation for galaxies (Koopmans et al. 2009), while it is likely not a sufficiently complex model to capture the lensing properties of massive galaxy clusters (Richard et al. 2010).

We use ray-tracing simulations to explore the impact of lens ellipticity and finite source sizes, assuming constant values of ellipticity and source sizes and exploring the impact of different assumed values.

In all that follows, we assume as our fiducial cosmology a spatially flat universe with $\Omega_m = 0.222$, $H_o = 71.0$ km/s/Mpc, $\Omega_b = 0.0449$, $n_s = 0.963$ and $\sigma_8 = 0.801$.

3. UNLENSED MM-WAVE NUMBER COUNT PREDICTIONS

The assumed unensed source count models (the Durham and UBC models) have not been calibrated at mm wavelengths; small differences in parameters such as dust emissivity that are not large effects at submm wavelengths could lead to large misestimates at mm wavelengths.

A simple check is to verify that the models produce a reasonable amount of noise power in mm-wave maps; this has been measured in SPT data in Hall et al. (2009). We computed the angular noise power, defined for randomly distributed point sources as

$$c_l = \int_0^{S_{cut}} S^3 \frac{dN}{dS} d(\ln S) \quad (1)$$

with a flux cut-off of 17 mJy (Hall et al. 2009) for SPT at 220 GHz (1.4 mm). The majority of the noise power comes from sources well below the SPT sensitivity limit for detecting individual sources.

The noise power from the UBC model is in excellent agreement with the measurements, and didn't require any corrections. The noise power derived from the Durham model, around $60 \text{ Jy}^2/\text{sr}$, is more than a factor of 3 too high compared to Hall et al. (2009). We scale the flux of each object by a constant amount to match the measured noise power. In Figure 1 it can be seen that the Durham and UBC models are forced by this constraint on the total power to have comparable number counts at fluxes of a few mJy.

After applying a constant flux correction to match the observed noise power, the Durham model still had a problem with the properties of low-redshift dusty galaxies, in that the predicted number of low-redshift galaxies in the SPT sample was too high. In particular, the brightest of the low-z population in the Durham model (observed by IRAS) are predicted to be bright enough in the SPT maps to be found as sources. This is not the case, as evidenced by the small fraction of SPT-discovered galaxies that were also observed to be IRAS sources (Vieira et al. 2010)¹. As gravitational lensing is more efficient for high redshift sources, we elected to simply further suppress the flux of low-z galaxies ($z < 0.2$)

to make the low-z galaxy counts agree with the number of SPT sources found to coincide with IRAS sources. While not rigorously justifiable, the main point of using the Durham model was to get a plausible redshift distribution of sources at high-redshift. In order to avoid misinterpretations caused by the low-z population we only apply our lensing model to Durham counts with $z > 0.2$ eliminating the low redshift counts and compare the results to SPT's IRAS removed counts.

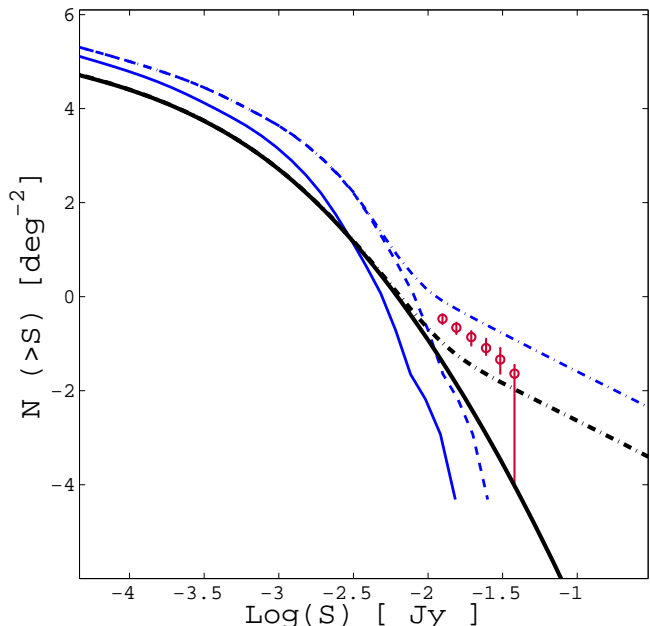


FIG. 1.— Unensed number count predictions for SPT sources at 220 GHz. The thin dash-dotted blue line shows the original Durham counts while the thin dashed blue curve shows the same counts with $z > 0.2$. The thin solid blue curve is the Durham model corrected to match the measured noise power (Hall et al. 2009). The thick black dashed line shows the total UBC counts and the thick solid black line is UBC with $z > 0.2$ for comparison purposes. The data points are 220 GHz (1.4 mm) SPT dusty galaxies after removing known IRAS sources (Vieira et al. 2010).

4. GRAVITATIONAL LENSING THEORY

For the details of gravitational lensing theory we refer the reader to a review by (Bartelmann & Schneider 2001). Here we only briefly state a few lensing quantities that are used in this work. The lens equation that we solve numerically is written as

$$\vec{\beta} = \vec{\theta} - \frac{D_{ds}}{D_s} \hat{\alpha}(D_d \vec{\theta}) = \vec{\theta} - \vec{\alpha}(\vec{\theta}) \quad (2)$$

where D_d , D_s , and D_{ds} are the angular diameter distances of deflector (d) and source (s) and $\vec{\beta}$ is the observed position of a point source at $\vec{\theta}$ deflected by an angle $\vec{\alpha}$. The total deflection from an ensemble of point masses at a single lens plane is given by

$$\hat{\alpha}(\vec{\theta}) = \frac{1}{\pi} \int d^2\theta' \kappa(\vec{\theta}') \frac{\vec{\theta} - \vec{\theta}'}{|\vec{\theta} - \vec{\theta}'|^2} \quad (3)$$

¹ <http://pole.uchicago.edu/public/data/vieira09/index.html>

The dimensionless surface mass density κ is

$$\kappa(\vec{\theta}) = \frac{\Sigma(D_d\vec{\theta})}{\Sigma_{cr}} \quad \text{where} \quad \Sigma_{cr} = \frac{c^2}{4\pi G} \frac{D_s}{D_d D_{ds}} \quad (4)$$

where Σ_{cr} is the critical surface mass density and $\Sigma(\vec{\xi})$ is the 2D projected mass density of the lens.

5. LENS MODELING AND CALCULATION DETAILS

5.1. Ray-tracing

The lens equation (Eq. 2) is an implicit equation, in that the image position $\vec{\theta}$ is needed to evaluate the deflection $\vec{\alpha}(\vec{\theta})$. For a given source position $\vec{\beta}$ it is difficult to solve this implicit equation to obtain $\vec{\theta}$. On the other hand, if $\vec{\theta}$ is known $\vec{\beta}$ can be easily evaluated. This constitutes the basis of ray-tracing simulations of gravitational lensing: start with an array of image positions and determine the source positions from which they emerged.

Simple halo profiles, like the singular isothermal sphere (SIS), can often produce analytical cross-sections. More complex mass profiles often have no simple analytical solution and the cross-section has to be numerically computed using a ray tracing simulation. In addition to the ability to compute lensing quantities for any arbitrary mass configuration, ray-tracing simulations have the advantage that they can easily include finite source effects which are not properly modeled in analytical solutions.

Our simulation makes surface density maps as a matrix of 400×400 elements and solves the lens equation using the method described in (Keeton 2001). The image plane is divided to 180×180 squares each of which is divided into two triangles and the corresponding positions of each vertex are found in the source plane. The magnification is computed by defining a grid in the source plane and calculating the image-plane area of triangles that have been mapped into each source position.

5.2. Halo Mass Profile and Ellipticity

We assume that the lens profiles in the region of interest are well-approximated by singular isothermal profiles, where the three dimensional density profile for a spherical profile is

$$\rho(r) = \frac{\sigma_\nu^2}{2\pi G r^2} \quad (5)$$

where σ_ν is the line-of-sight velocity dispersion of the stars in the galactic disk or the galaxies in a galaxy cluster. It is well known that this is not a good approximation to halos produced in dark matter simulations (Navarro et al. 1997), but the region that dominates the strong lensing properties is typically dominated by baryonic processes and is empirically found to be close to isothermal (Koopmans et al. 2009).

The dependence of the velocity dispersion on the redshift and mass of the halo is given by Bryan & Norman (1998) as

$$\sigma_\nu = f_\sigma M^{1/3} \left[\frac{H^2(z)\Delta(z)G^2}{16} \right]^{1/6} \quad (6)$$

where

$$\Delta(z) = 18\pi^2 + 82(\Omega_m - 1) - 39(\Omega_m - 1)^2 \quad (7)$$

and f_σ is a scaling parameter used to match the normalization from simulations. While the density profile may indeed scale roughly as $1/r^2$ in the central regions of interest, the relationship between the normalization (i.e., the velocity dispersion) and total halo mass is not empirically calibrated and is a potential large source of systematic uncertainty in this analysis.

Integrating $\rho(r)$ along the line-of-sight produces the projected surface mass density

$$\Sigma(\xi) = \frac{\sigma_\nu^2}{2G\xi} \quad (8)$$

The corresponding dimensionless surface mass density is

$$\kappa(\theta) = \frac{\theta_E}{2\theta} \quad (9)$$

where we have defined the Einstein deflection angle as

$$\theta_E = 4\pi \left(\frac{\sigma_\nu}{c} \right)^2 \frac{D_{ds}}{D_s} \quad (10)$$

The magnification for point sources lensed by this mass profile is analytic, with $\mu(\vec{\theta}) = |\vec{\theta}|/(|\vec{\theta}| - \theta_E)$. We calculate magnification for extended sources as the ratio of the area of combined images to the source area. This allows easy exploration of finite source effects and non-trivial lens distributions.

The integral lensing cross-section $\sigma(\mu > \mu_{min})$ is the area on the source plane inside which the magnification of a source is equal or larger than μ_{min} . Throughout this work the $\sigma(\mu > \mu_{min})$ and $\sigma(\mu)$ are used interchangeably. The cross-section for an SIS halo for $\mu_{min} > 2$ is given analytically by Perrotta et al. (2002) and at large magnifications our numerical results agree with the analytic form to better than 2.5%.

The morphology of the galaxies from observations (Evans & Bridle 2009) and the shape of dark matter halos from N-body simulations (Ludlow et al. 2010) both indicate that a considerable amount of ellipticity is present in the lensing halos. Many studies before (e.g. Meneghetti et al. (2005)) have introduced ellipticity in the projected two-dimensional lensing potential ϕ . For analytical studies this has the advantage that the second derivatives of the potential give the lensing quantities directly and lead to simple analytical expressions. However for high values of ellipticity this implies dumbbell shape density profiles which are unrealistic. Simulations and observations both indicate ellipticity in the distribution of mass, rather than in the potential resulting from it. In our ray-tracing approach it is simple to introduce ellipticity in the actual surface mass density. At each point defined by x and y on the two-dimensional plane with radius $r = \sqrt{x^2 + y^2}$ we compute the SIS or NFW density using radius r_e defined as

$$r_e = \sqrt{\frac{x^2}{1 - e_\kappa} + y^2(1 - e_\kappa)} \quad (11)$$

The axis ratio are now given by $b/a = 1 - e_\kappa$.

The impact of ellipticity can be clearly seen in Figure 2. Ellipticity increases the area of the source plane where strong lensing can occur. However, in this same figure we can see the effects of finite sources. The regions

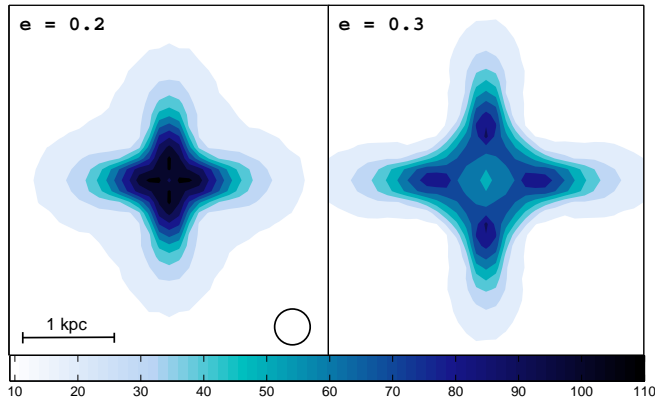


FIG. 2.— Magnification maps of two halos with identical total mass ($M = 10^{13} M_{\odot}$) and different ellipticities ($e_{\kappa} = 0.2$ for the left panel and $e_{\kappa} = 0.3$ for the right panel). The extended circular source (drawn as a black circle) is identical in both plots making all magnification differences due to ellipticity. The left panel contains large magnifications in excess of $\mu = 100$ which are damped in the right panel. But intermediate magnifications are extended to larger regions in the right panel.

of high magnification become narrower as ellipticity increases, so larger sources will tend to have smaller peak magnifications.

The interplay between ellipticity and source size is shown in Figure 3. Ellipticity generally leads to higher magnifications, but finite source sizes become more important for higher ellipticity. This discussion has assumed a fixed Einstein radius. The relevant factor is the ratio of the source size to the Einstein radius; a given source size that may be a problem for a galaxy-scale lens would behave like a point source for the purposes of lensing by a galaxy cluster.

At intermediate magnifications, finite source effects tend to increase the lensing cross-section. This occurs because sources are now occupying a larger fraction of the source plane and are more likely to have a part of the emitting region be in the strong lensing regime.

5.3. Probability function

We use the halo mass function of Sheth & Tormen (1999) to determine the number of halos of a given mass at each redshift, and we sum the source plane cross-sections of all lenses between the observer and source, dividing by the total area of the sphere centered at the observer with a radius at the source redshift. This is the probability that a source at that redshift is magnified by at least μ due to all intervening halos.

The sum of all cross-sections in a flat Universe can be written as

$$\sigma_{tot}(\mu, z_s, R_s, e_{\kappa}) = 4\pi \left(\frac{c}{H_o} \right) \int_0^{z_s} dz_d \quad (12)$$

$$\int dM \frac{\sigma(\mu, z_d, z_s, M, R_s, e_{\kappa}) n_c(z_d, M) (1+z_d)^2 D^2(z_d)}{\sqrt{\Omega_{oM}(1+z_d)^3 + \Omega_{o\Lambda}}}$$

where $n_c(z_d, M)$ is the number density of lenses of mass M at redshift z_d and $D(z_d)$ is the angular diameter distance at redshift z_d .

Using the assumed mass and redshift scalings for our assumed isothermal halo profile, to find the cross-section for each lens as a function of mass M and redshift z_d we

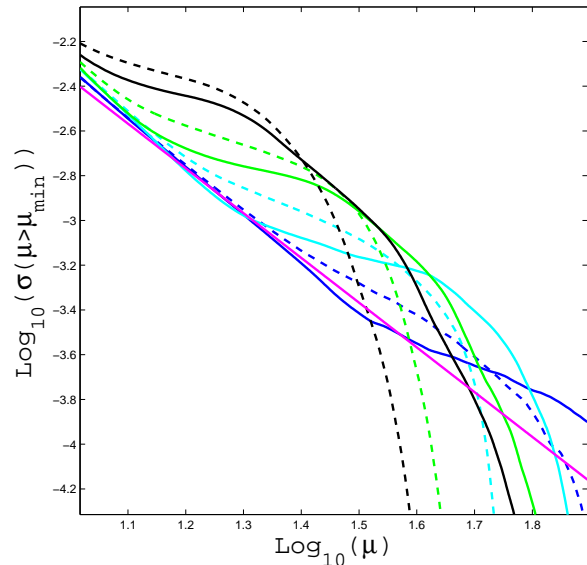


FIG. 3.— The above curves demonstrate the correlation of finite source effects with halo ellipticity. As halos become more elliptical they become more sensitive to finite source effects and dampen faster at high magnification. The colors correspond to different lens halo ellipticities: blue, cyan, green, and black correspond to $e_{\kappa} = 0.1$, $e_{\kappa} = 0.2$, $e_{\kappa} = 0.3$, and $e_{\kappa} = 0.4$ respectively. Solid lines are the cross-sections for a source with a radius of $0.023 R_{Ein}$ while dashed lines correspond to a $0.041 R_{Ein}$ radius source.

can use the following scaling relation

$$\sigma(\mu, z_d, z_s, M, R_s, e_{\kappa}) = \quad (13)$$

$$\left[\frac{M}{M_0} \right]^{4/3} \left[\frac{D_{ds}/D_s}{D_{ds,0}/D_{s,0}} \right]^2 \chi^2(z_d) \sigma_0(\mu, \frac{R_s}{R'_E}, \epsilon)$$

where the subscript 0 refers to the quantities for a normalization halo from which the cross-section for other halos are achieved by the above scaling relation. R'_E is the Einstein radius of the scaled halo and σ_0 is a look-up table of the cross-sections as a function of halo ellipticity and source-size to Einstein radius ratio. $\chi(z_d)$ is the scaling factor due to the dependence of the halo velocity dispersion, σ_v on redshift and is given by

$$\chi(z_d) = \left(\frac{H^2(z_d) \Delta(z_d)}{H^2(z_{d,0}) \Delta(z_{d,0})} \right)^{1/3} \quad (14)$$

The probability that a source at z_s is magnified by a factor greater than μ_{min} is then

$$P(\mu > \mu_{min}) = \frac{\sigma(\mu > \mu_{min})}{4\pi D_s^2} \quad (15)$$

5.4. Lensed Number Counts

Gravitational lensing conserves the surface brightness of the lensed sources. Consequently any sources magnified by a factor of μ are also μ times brighter. In addition to making sources appear brighter, gravitational lensing also dilutes the source populations by magnifying the observed solid angles. Therefore it also dilutes the number counts by a factor of μ .

As discussed extensively in Jain and Lima (2009), these effects can be combined for a large survey to obtain the

observed number counts as

$$\frac{dn}{dS} = \int \int \frac{1}{\mu'} \frac{dP}{d\mu'}(\mu', z) \frac{d\hat{n}}{d\hat{S}}(\hat{S} = \frac{S}{\mu'}, z) dz d\mu' \quad (16)$$

where we denoted the observed flux as S and the unlensed flux as \hat{S} , such that $S = \mu\hat{S}$ and the unlensed differential source sky density as $d\hat{n}/d\hat{S}$.

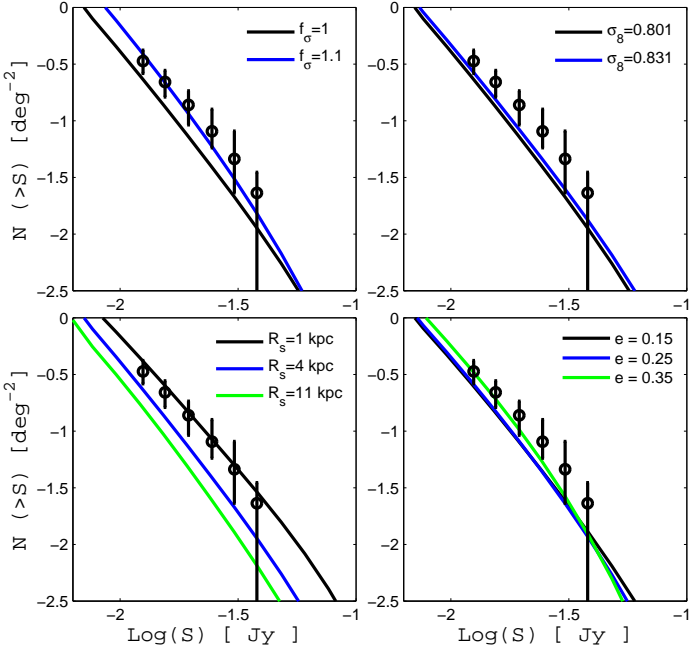


FIG. 4.— The above plots demonstrate the effects of several parameters on the predicted number counts. Top-left, top-right, bottom-left, and bottom-right panels respectively show the effects of $\sigma_\nu(M)$, σ_8 , source size, and ellipticity. All other parameters are fixed in each panel ($f_\sigma = 1$, $\sigma_8 = 0.801$, $R_s = 4 \text{ kpc}$, and $e = 0.15$)

The four panels in Figure 4 shows the lensed count predictions for SPT as the most relevant parameters are varied. The cosmological uncertainty is clearly subdominant to uncertainties in the source properties and lens properties. In particular, the overall normalization of the mass profiles (f_σ) and the source size can change the expected number of strong lenses by large amounts.

Figures 5 and 6 illustrates that there are lensing models which fit the SPT source counts quite well for both the Durham and UBC unlensed source count models. The lensing parameters are slightly different, with the Durham model preferring slightly larger source sizes and smaller ellipticity. The contribution of various redshift ranges to the lensed number counts can also be seen to be slightly different for the two models: Figure 5 shows that the Durham model finds that most of the sources lie at $z \gtrsim 3$ over the entire SPT flux range, while Figure 6 shows that the UBC model has a significant fraction of lensed sources as low as $z \sim 2$.

In Figures 7 and 8, the distribution in magnification can be seen to be a strong function of flux for both models. At the low-flux end the cross-section is dominated by relatively low magnifications (~ 10), while higher fluxes are increasingly dominated by larger magnifica-

tions. This isn't surprising, given the steep unlensed luminosity function.

The mean magnification at different fluxes is seen to have significant differences between the Durham and UBC models, suggesting that this could be a useful diagnostic for reconstructing the unlensed luminosity function. In Figure 7 the Durham model is largely dominated by the highest magnifications in the region of the SPT counts, while Figure 8 shows that the UBC model shows a transition from low magnification to high magnification in the flux range where SPT has reported constraints. This is a direct reflection of the differences in the unlensed counts: the Durham model has an abrupt fall-off at the high flux end of the unlensed counts, well below the flux range probed by SPT, while the UBC model has more unlensed high redshift bright objects.

6. DISCUSSION AND CONCLUSIONS

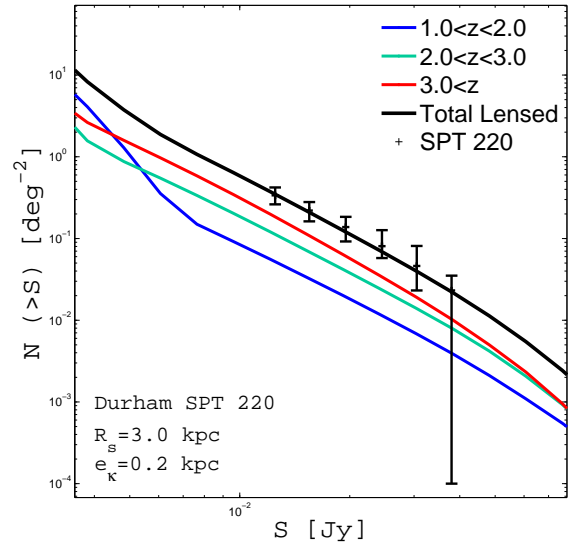


FIG. 5.— Best-fit lensed counts for SPT 220 GHz for Durham model. The lensing consists of halos with $e_{\kappa} = 0.2$ and $R_s = 3 \text{ kpc}$. The colored curves show the contribution of each redshift bin to the total counts. The unlensed counts only include sources with $z > 0.2$ and the data points are SPT 220 dust counts with IRAS counterparts removed.

The observed number counts of galaxies at mm wavelengths is easily explained by gravitational lensing. However, the predictions for the number counts have several large sources of uncertainty, several of which we have explored in some detail.

The physical size of sources is an important factor in determining the amount of magnification. This has been an important source of uncertainty in previous calculations (Paciga et al. 2009). Mathematical point sources can be treated analytically, but for any realistically extended source the magnification can be strongly affected. For large sources (compared to the lens Einstein radius) the maximum magnification is considerably reduced. As the relevant scale is the Einstein radius (a property of the lens), this effect will depend strongly on the mass of the lens. At intermediate magnifications (i.e. $10 < \mu < 40$) finite source effects can *increase* the lensing cross-section because larger sources have higher probability of having

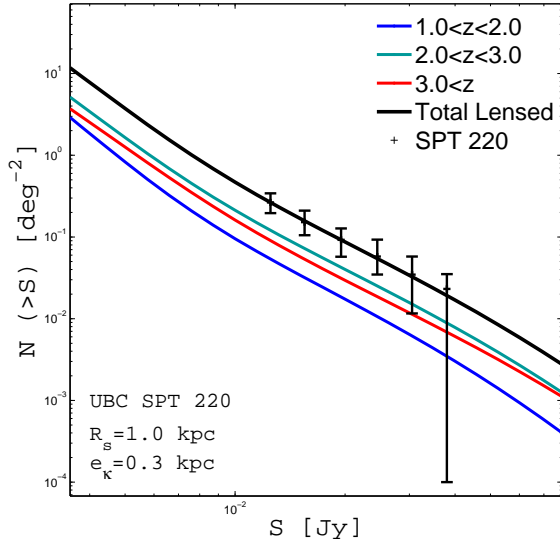


FIG. 6.— Same as plot 5 for UBC model with $e_\kappa = 0.3$ and $R_s = 1 \text{ kpc}$.

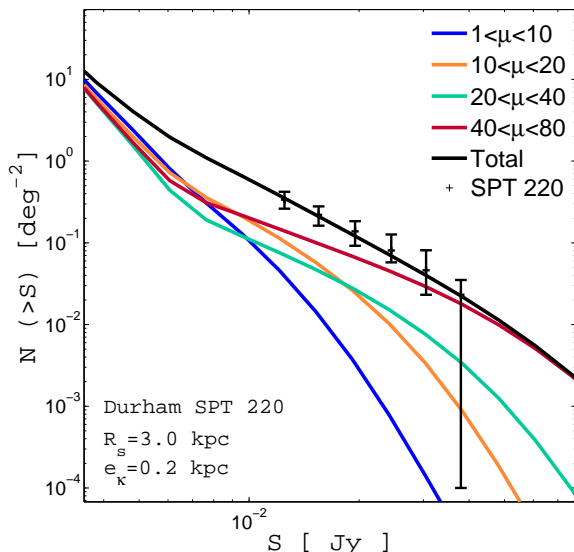


FIG. 7.— Magnification breakdown of the predicted SPT 220 GHz lensed counts for Durham model.

a part of them fall within the inner caustics and be highly magnified.

For the Durham model we observe that allowing sources with radius larger than 5 kpc leads to predicted counts falling below the observations. While it is not expected that the massively star-forming region in these sources is significantly larger than this, this is another observational clue to the physical processes in these galaxies. This has already been measured observationally for individual sources (Momjian et al. 2010). More extensive future follow-up observation of more SMG lensed sources could give better observational constraints on the range of SMG sizes.

Ellipticity is important in two ways: it increases the total area of high magnification by increasing the area of the so-called “diamond caustic,” but it also leads to more sharply-defined structures in the source plane, making

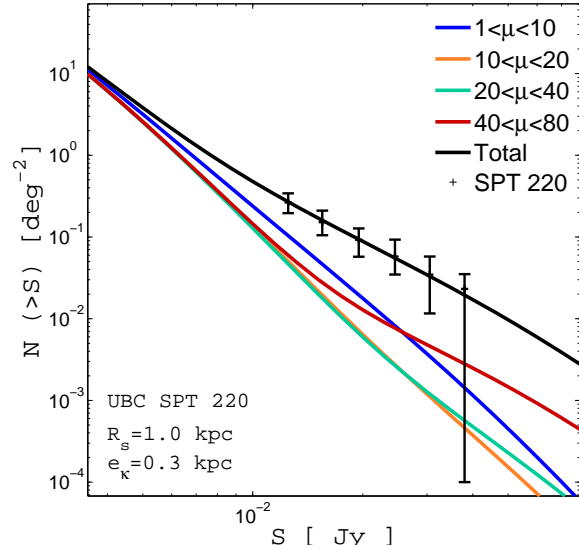


FIG. 8.— Same as plot 7 for UBC counts.

finite source size effects more important. The trade-off between these effects was found to be an important effect, as this can change the local slope of the lensed number counts.

A more realistic approach would be to assume a distribution of ellipticities and source sizes to constrain the parameter space. However, with the strong parameter degeneracies we have identified it is clear that more data will be required to separate these effects.

There remains significant uncertainty in the expected redshift distribution of the sources that comprise the mm-wave background from star-forming galaxies. Gravitational lensing provides a magnified view of these objects, providing an opportunity to probe the star formation history. As a measure of the source redshift distribution we have plotted the lensed number counts in several bins in Figures 5 and 6. The redshift distribution clearly depends on flux and the details of the assumed unlensed population.

Source redshift distribution is an important indicator of the nature of submm populations. The recent SPT observations by Vieira et al. (2010) show a large population of mm sources which were previously unseen in other catalogues. These sources are speculated to be high-redshift gravitationally lensed galaxies. Our lensed number count plots suggest that this can be a possible scenario. Figures 5 and 6 show that sources with redshifts larger than $z > 3$ (red curve) constitute at least half of the observed non-IRAS-detected dusty sources of Vieira et al. (2010).

Throughout this work we have assumed SIS profiles as the mass model for lensing halos. Strong lensing is very sensitive to the inner structure of the halos very close to the center (Mead et al. 2010). Rotation curves of galaxies which are approximately flat to large distances (Rubin & Ford 1970) suggest that such a model is not a bad approximation to the mass density profile of galaxy-sized halos. While this is not likely to be a bad approximation even up to cluster scales, the normalization of the mass density profile may not be expected to follow the self-similar scaling expected for the large-scale velocity dispersion of the dark halo. Given the strong sensitivity

to the overall normalization of the density profile seen in Figure 4, strong lensing number counts will be sensitive to the details of the radial profiles of the mass density and its evolution with mass.

A more realistic calculation would involve taking an NFW halo (Navarro et al. 1997), correcting for baryonic condensation at the center, and populating it with smaller subhalos according to galaxy occupation numbers (Oguri 2006). The positioning of the subhalos could be an important factor, as would the density profiles of the substructure. A similar work was done by Meneghetti et al. (2003) where the effects of a cD galaxy on the cross-section of the main halo has been examined. This could perhaps be better resolved by carrying out ray-tracing simulations through N-body simulations which include realistic baryonic matter. Such a work has been carried out by Hilbert et al. (2007) where they study ray-tracing through the Millennium simulation; they include baryonic matter based on semi-analytic models of star formation in a related study (Hilbert et al. 2008). These studies have not had the required resolution at galaxy-scale levels to study strong lensing due to substructure. In general, there is very little empirical guidance at this time for connecting Einstein radius to halo mass for halos smaller than galaxy clusters; population studies of strong lenses may provide some of the best constraints.

The methods used here can be generally applied to number count predictions for observations with other instruments such as Herschel (operating at 250, 350, and 500 μm), BLAST, etc. The large sky coverage of SPT makes it particularly efficient, probing the rarest objects, where a large fraction are strongly lensed. On the other hand, the deeper Herschel observations allow counts to lower fluxes, allowing better characterization of the unlensed source distribution. A combined analysis of Herschel and SPT lensed counts will provide key insights into properties of both gravitational lenses and star-forming galaxies at high redshift. The results of Vieira et al. (2010) were based on less than 10% of the final projected SPT survey area, and the Herschel observations are just now starting to emerge. The upcoming Atacama Large Millimeter Array will have the resolution to make detailed images of these sources, providing more precise observational constraints on theoretical models presented here.

We thank Joaquin Vieira and Bhuvnesh Jain for useful conversations, and Cedric Lacey and Gaelen Marsden for providing unpublished source count models at SPT wavelengths. This work was supported by the Canadian Institute for Advanced Research, as well as NSERC Discovery and the Canada Research Chairs program.

REFERENCES

- Bartelmann, M., & Schneider, P. 2001, *Phys. Rep.*, 340, 291
 Baugh, C. M., Lacey, C. G., Frenk, C. S., Granato, G. L., Silva, L., Bressan, A., Benson, A. J., & Cole, S. 2005, *MNRAS*, 356, 1191
 Blain, A. W. 1998, *MNRAS*, 297, 511
 Blain, A. W., Smail, I., Ivison, R. J., Kneib, J., & Frayer, D. T. 2002, *Phys. Rep.*, 369, 111
 Bryan, G. L., & Norman, M. L. 1998, *ApJ*, 495, 80
 Coppin, K., et al. 2006, *MNRAS*, 372, 1621
 Evans, A. K. D., & Bridle, S. 2009, *ApJ*, 695, 1446
 Frayer, D. T., et al. 2010, *ArXiv e-prints*
 Hall, N. R., et al. 2010, *ApJ*, 718, 632
 Hilbert, S., White, S. D. M., Hartlap, J., & Schneider, P. 2007, *MNRAS*, 382, 121
 —. 2008, *MNRAS*, 386, 1845
 Jain, B., & Lima, M. 2010, *ArXiv e-prints*
 Keeton, C. R. 2001, *ArXiv Astrophysics e-prints*
 Koopmans, L. V. E., et al. 2009, *ApJ*, 703, L51
 Lacey, C. G., Baugh, C. M., Frenk, C. S., Benson, A. J., Orsi, A., Silva, L., Granato, G. L., & Bressan, A. 2010, *MNRAS*, 405, 2
 Lima, M., Jain, B., & Devlin, M. 2009, *ArXiv e-prints*
 Lima, M., Jain, B., Devlin, M., & Aguirre, J. 2010, *ArXiv e-prints*
 Ludlow, A. D., Navarro, J. F., Springel, V., Vogelsberger, M., Wang, J., White, S. D. M., Jenkins, A., & Frenk, C. S. 2010, *MNRAS*, 406, 137
 Mead, J. M. G., King, L. J., Sijacki, D., Leonard, A., Puchwein, E., & McCarthy, I. G. 2010, *MNRAS*, 406, 434
 Meneghetti, M., Bartelmann, M., Dolag, K., Perrotta, F., Baccigalupi, C., Moscardini, L., & Tormen, G. 2005, *NewAR* 49, 111
 Meneghetti, M., Bartelmann, M., & Moscardini, L. 2003, *MNRAS*, 340, 105
 Michałowski, M., Hjorth, J., & Watson, D. 2010, *A&A*, 514, A67+
 Momjian, E., Wang, W., Knudsen, K. K., Carilli, C. L., Cowie, L. L., & Barger, A. J. 2010, *AJ*, 139, 1622
 Navarro, J. F., Frenk, C. S., & White, S. D. M. 1997, *ApJ*, 490, 493
 Negrello, M., Perrotta, F., González-Nuevo, J., Silva, L., de Zotti, G., Granato, G. L., Baccigalupi, C., & Danese, L. 2007, *MNRAS*, 377, 1557
 Oguri, M. 2006, *MNRAS*, 367, 1241
 Paciga, G., Scott, D., & Chapin, E. L. 2009, *MNRAS*, 395, 1153
 Perrotta, F., Baccigalupi, C., Bartelmann, M., De Zotti, G., & Granato, G. L. 2002, *MNRAS*, 329, 445
 Press, W. H., & Schechter, P. 1974, *ApJ*, 187, 425
 Richard, J., et al. 2010, *MNRAS*, 404, 325
 Rubin, V. C., & Ford, Jr., W. K. 1970, *ApJ*, 159, 379
 Sheth, R. K., & Tormen, G. 1999, *MNRAS*, 308, 119
 Turner, E. L., Ostriker, J. P., & Gott, III, J. R. 1984, *ApJ*, 284, 1
 Vieira, J. D., et al. 2010, *ApJ*, 719, 763